

# Critical evaluation of PINN for FWD inverse analysis and differentiable FEM as an alternative

Yongjin Choi<sup>a,c,1</sup>, Hyeonbin Moon<sup>b,1</sup>, Seunghwa Ryu<sup>a,b,\*</sup>

<sup>a</sup>*KAIST InnoCORE PRISM-AI Center, Korea Advanced Institute of Science and Technology (KAIST), Daejeon, 34141, Republic of Korea*

<sup>b</sup>*Department of Mechanical Engineering, Korea Advanced Institute of Science and Technology (KAIST), Daejeon, 34141, Republic of Korea*

<sup>c</sup>*School of Civil and Environmental Engineering, Georgia Institute of Technology, Atlanta, 30332, GA, USA*

---

## Abstract

Automatic-differentiation-based inverse analysis methods, including physics-informed neural networks (PINNs) and differentiable programming, have recently shown great promise due to their ability to compute accurate gradients and convergence efficiency. However, their applicability to falling weight deflectometer (FWD) backcalculation remains unexplored. This study critically evaluates PINN-based inverse analysis for a multilayer pavement system and investigates differentiable finite element method (DiffFEM) as an alternative based on a synthetic benchmark. The standard PINN does not recover layer moduli because of the sharp domain discontinuities inherent to layered pavement systems. Although we use an extended PINN with domain decomposition (XPINN), which shows better performance on discontinuous domains, its performance remains highly sensitive to loss weighting and network architecture, and degrades under measurement noise. By contrast, DiffFEM consistently achieves more accurate, stable, and computationally efficient inversion results. These results indicate that DiffFEM, which enforces the governing physics as a hard constraint, yields better accuracy, robustness, and computational efficiency than PINN-based approaches, in which the governing physics is imposed as a soft constraint through the loss function. More broadly, the findings suggest that the choice between PINN- and DiffFEM-based inverse analysis needs careful consideration, with DiffFEM offering practical advantages when an efficient and robust differentiable forward solver is available.

*Keywords:* Inverse problems, Automatic differentiation, Differentiable programming, Physics-informed neural networks, Falling weight deflectometer

---

## 1. Introduction

The falling weight deflectometer (FWD) (Smith et al., 2017) is a widely used device for non-destructive structural evaluation of pavement systems. In an FWD test, an impulse load is applied

---

\*Corresponding author

*Email address:* ryush@kaist.ac.kr (Seunghwa Ryu)

<sup>1</sup>These authors contributed equally to this work.

at the pavement surface, and an array of geophones records the resulting deflection basin. This measured basin is then used to backcalculate layer moduli through an iterative optimization process: a forward model predicts the deflection basin for a candidate set of moduli, and the moduli are updated until the predicted response matches the measurements.

Within the quasi-static, layered elastic framework, early efforts approached this inverse problem using database search optimization, as in MODULUS (Rohde and Scullion, 1990), or sampling-based techniques (Zhang et al., 2003). These methods, however, either compromise generality or become computationally inefficient as the number of layer moduli increases. Gradient-based approaches, such as EVERCALC (Harichandran et al., 1993), provide faster convergence with flexibility in formulation. Yet, despite their widespread use, these methods share a fundamental numerical limitation: gradients are typically computed via finite-difference (FD) approximations. From a computational standpoint, this requires at least  $N$  additional forward simulations per iteration for  $N$  unknown layer moduli, leading to poor scalability and reduced efficiency as the number of layers increases. In addition, FD gradient approximations introduce truncation errors that are sensitive to the choice of perturbation step size, potentially degrading the quality of the computed gradients (Choi and Kumar, 2024) and consequently to the stability of the back-analysis. These limitations naturally motivate more principled and efficient approaches to gradient evaluation.

Automatic differentiation (AD) (Margossian, 2019; Paszke et al., 2017) offers a principled alternative by enabling efficient and accurate gradient computation through a single backward pass, thereby avoiding the truncation errors and scalability limitations of FD. Physics-informed neural networks (PINNs) (Raissi et al., 2019) are a prominent framework built on this capability, in which the governing equations are embedded into the loss function of a neural network. In inverse analysis, the unknown parameters are treated as trainable variables together with the network weights and are inferred by minimizing a composite loss of governing-equation residuals and data misfit, enabling physics-constrained inversion. Motivated by these advantages, PINNs have attracted growing attention in geotechnical forward and inverse problems (Yuan et al., 2025), including soil parameter identification (Bekele, 2021) and subsurface characterization (Rasht-Behesht et al.,

2022). However, their applicability to multilayered pavement inverse analysis for FWD remains largely unexplored.

Despite their promise, PINNs present notable practical challenges. Their training is often sensitive to hyperparameter choices, including network architecture, learning rate, and the relative weighting between governing-equation residuals and data misfit in the multi-objective loss function (Faroughi et al., 2024; Chou et al., 2025; Kumar, 2025). Poor choices of these hyperparameters can lead to non-convergence or suboptimal solutions (Kumar, 2025), while the practical implications of this sensitivity, including computational cost, are not always made fully explicit. In addition to these general training issues, FWD backcalculation introduces a problem-specific difficulty. Pavement systems consist of discrete layers with sharp modulus discontinuities at their interfaces, which correspond to high-frequency features in the solution space. Standard PINNs are known to exhibit spectral bias, that is, a tendency to learn low-frequency components more easily than sharp transitions (Naser, 2025; Peng and Panesar, 2025). This limitation may degrade the representation of interlayer behavior and, in turn, the accuracy and robustness of inversion. Although Fourier feature embedding can mitigate spectral bias by enhancing high-frequency representation (Liu et al., 2025), they are more effective for smooth multiscale variations than for sharp material discontinuities (Fazliani et al., 2025). It therefore remains unclear whether PINN-based methods can solve multilayered pavement inverse problems reliably and efficiently.

These challenges highlight a more fundamental issue: while PINNs leverage AD for efficient gradient computation, they rely on a neural network surrogate that only approximately satisfies the governing equations through a loss function and requires problem-specific modifications. This raises the question of whether the advantages of AD can be retained within a framework that directly enforces the underlying physics. Differentiable programming (Hu et al., 2019; Innes et al., 2019) provides such a possibility. By embedding the finite element method (FEM) forward solver within an AD framework, yielding differentiable FEM (DiffFEM), the gradient of surface deflections with respect to layer moduli can be obtained through a backward pass, while the governing physics are enforced through the FEM at every iteration. In this way, DiffFEM retains a physics-native forward model rather than introducing a neural surrogate. This formulation also avoids the interface-

representation difficulty associated with neural network surrogates. These considerations motivate the investigation of DiffFEM as a physics-consistent alternative for multilayered pavement inverse analysis.

This study critically evaluates the applicability of PINN-based approaches to FWD backcalculation and investigates DiffFEM as a physics-consistent, AD-based alternative. Specifically, we first examine the performance of a vanilla PINN in recovering pavement moduli in a multilayered system. Recognizing that the single-network PINN struggles with the multilayered pavement system with modulus discontinuities, we then adopt an extended PINN formulation with domain decomposition (XPINN) (Jagtap and Karniadakis, 2020), in which each pavement layer is represented by a separate sub-network. This progression from a standard PINN to a problem-adapted XPINN allows us to evaluate PINN-based inversion under a formulation that is more suitable for the layered structure of pavements. Finally, we compare these PINN-based approaches with DiffFEM to identify which AD-based inverse analysis framework is more appropriate for multilayered pavement backcalculation. Overall, these findings provide a comparative assessment of PINN-based and physics-native differentiable simulation-based approaches and offer practical discussion for their use in multilayered pavement inverse analysis.

## 2. FWD backcalculation background

### 2.1. Test procedure and inverse problem

The falling weight deflectometer (FWD) applies a controlled impulse load to the pavement surface and records the resulting deflection basin at an array of geophones positioned at fixed radial offsets from the load center. Following established practice (Smith et al., 2017; Von Quintus et al., 2015), peak deflection values are used for structural analysis under a quasi-static, layered elastic assumption—a setting shared by many backcalculation software, including EVERCALC (Harichandran et al., 1993), and MODULUS (Von Quintus et al., 2015).

Under Burmister’s layered elastic theory (Burmister, 1945), the surface deflections at the  $m$  geophone locations are a nonlinear function of the unknown layer moduli  $\mathbf{E} = [E_1, \dots, E_n]^\top$ , given known layer thicknesses, Poisson’s ratios, and loading conditions (Equation (1)).

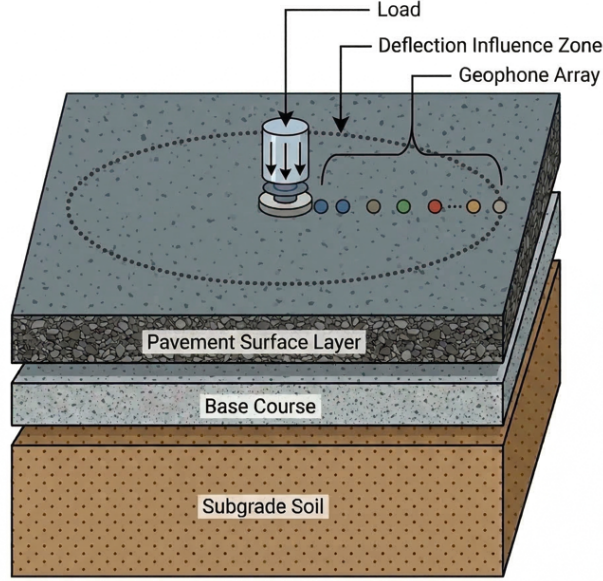


Figure 1: Schematic of the falling weight deflectometer (FWD) test on a layered pavement system. An impulse load is applied at the surface, and the resulting deflection basin is recorded by an array of geophones at increasing radial offsets from the load center.

$$\mathbf{u} = \mathcal{F}(\mathbf{E}), \quad \mathbf{u} = [u_1, \dots, u_m]^\top \quad (1)$$

where  $\mathcal{F} : \mathbb{R}^n \rightarrow \mathbb{R}^m$  denotes the forward solver that maps the modulus vector to the predicted deflection basin, and  $u_j$  is the peak deflection at radial offset  $r_j$ .

Backcalculation seeks  $\mathbf{E}^*$  that minimizes the residual  $\ell$  between simulated and measured deflections (Equation (2)).

$$\mathbf{E}^* = \arg \min_{\mathbf{E}} \mathcal{L}(\mathbf{E}) = \frac{1}{m} \sum_{j=1}^m \ell(u_j(\mathbf{E}), u_j^{\text{obs}}) \quad (2)$$

where  $u_j(\mathbf{E})$  denotes the  $j$ -th component of  $\mathcal{F}(\mathbf{E})$ , and  $u_j^{\text{obs}}$  is the measured deflection at sensor  $j$ .

Existing approaches address Equation (2) via database search (Rohde and Scullion, 1990), sampling-based approaches (Gopalakrishnan and Manik, 2010; Zhang et al., 2003), ANN-based surrogates (Meier and Rix, 1994), or gradient-based iterative solvers (Harichandran et al., 1993). Among them, gradient-based methods exhibit highly efficient convergence behavior. However, existing implementations share a fundamental numerical limitation regarding scalability and stability,

which is discussed next.

## 2.2. Finite difference gradient approximation

Gradient-based optimization approaches iteratively updates  $\mathbf{E}$  based on the gradient information (Equation (3)) to solve the inverse problem defined in Equation (2).

$$\mathbf{E}^{(k+1)} = \mathbf{E}^{(k)} - \alpha^{(k)} \nabla_{\mathbf{E}} \mathcal{L}(\mathbf{E}^{(k)}) \quad (3)$$

where  $\alpha^{(k)}$  is the update step size at iteration  $k$ . Each step requires the gradient of the loss with respect to the layer moduli,  $\nabla_{\mathbf{E}} \mathcal{L} \in \mathbb{R}^n$ . When  $\mathcal{F}$  is evaluated numerically, getting this gradient as a closed-form expression is challenging, so typically estimated from a FD perturbation (Equation (4)).

$$[\nabla_{\mathbf{E}} \mathcal{L}]_i^{\text{FD}} = \frac{\mathcal{L}(\mathbf{E} + \Delta E_i \mathbf{e}_i) - \mathcal{L}(\mathbf{E})}{\Delta E_i} + \mathcal{O}(\Delta E_i) \quad (4)$$

where  $\mathbf{e}_i$  is the  $i$ -th unit vector and  $\Delta E_i$  is a user-chosen perturbation applied to modulus  $E_i$ .

This approximation has two limitations for multilayer pavement inversion. First, evaluating the full gradient requires one additional forward solve for each unknown modulus. For an  $n$ -layer system, one optimization step therefore requires  $n + 1$  forward evaluations: one baseline evaluation of  $\mathcal{L}(\mathbf{E})$  and  $n$  perturbed evaluations. The per-iteration cost thus scales linearly with the number of unknown moduli, which becomes increasingly expensive as more layers or sublayers are introduced.

Second, the FD gradient is only approximate. A large perturbation  $\Delta E_i$  increases truncation error, whereas a very small perturbation amplifies floating-point cancellation error (Press et al., 2007). As a result, the gradient quality depends strongly on the perturbation size, and no single choice is uniformly reliable across all layers. This issue is particularly important in FWD back-calculation, where the surface deflection basin can be only weakly sensitive to some deeper-layer moduli. In such cases, gradient inaccuracy can misdirect the update in Equation (3) and destabilize convergence.

Automatic differentiation, introduced next, addresses both drawbacks simultaneously.

### 2.3. Exact gradients via automatic differentiation

Automatic differentiation (AD) computes derivatives by differentiating the sequence of operations used in the forward computation itself. Rather than perturbing the input vector  $\mathbf{E}$  as in finite differences, AD applies the chain rule to the computational graph of the numerical solver. Because the derivatives of the elementary operations in that graph are known analytically, AD yields derivatives of the implemented forward model to machine precision, without finite-difference truncation error (Baydin et al., 2018).

For the inverse problem considered here, the quantity of interest is the gradient of the scalar loss  $\mathcal{L}$  with respect to the modulus vector  $\mathbf{E} \in \mathbb{R}^n$ . Reverse-mode AD is particularly well suited to this setting because one backward pass through the computational graph produces the full gradient with respect to all  $n$  unknown moduli:

$$\nabla_{\mathbf{E}} \mathcal{L} \xleftarrow{\text{1 backward pass}} \mathcal{L}(\mathcal{F}(\mathbf{E})), \quad (5)$$

In contrast to FD, the cost of this reverse pass does not grow linearly with the number of unknown moduli, making AD attractive for inverse problems with multiple parameters. This shared gradient mechanism underlies both PINN and DiffFEM, whose formulations are described next.

## 3. Methodology

### 3.1. Differentiable finite element method (DiffFEM)

Figure 2 illustrates the DiffFEM framework for pavement layer modulus backcalculation from FWD tests. The pavement domain is discretized into a two-dimensional axisymmetric finite element mesh using quadrilateral elements, with the radial coordinate  $r$  and depth coordinate  $z$  as the two spatial dimensions. For a three-layer system (surface course, base, and subgrade), the global stiffness matrix  $\mathbf{K} \in \mathbb{R}^{2N \times 2N}$ , where  $N$  is the total number of nodes and the factor of two accounts for the radial and vertical displacement degrees of freedom, admits a layer-additive decomposition (Equation (6)).

$$\mathbf{K}(\mathbf{E}) = \sum_{i=1}^{N_i} E_i \mathbf{K}^{(i)} \quad (6)$$

where  $N_i$  is the number of layers,  $E_i$  is the elastic modulus of layer  $i$ , and  $\mathbf{K}^{(i)}$  is the stiffness matrix assembled from the elements belonging to layer  $i$ .

With boundary conditions applied, the forward problem solves the linear system for the free degrees of freedom (Equation (7)).

$$\mathbf{K}_{\text{ff}}(\mathbf{E}) \mathbf{u}_f = \mathbf{F}_f \quad (7)$$

where the subscript  $f$  denotes free (unconstrained) degrees of freedom,  $\mathbf{u}_f$  is the solution vector of nodal displacements, and  $\mathbf{F}_f$  is the corresponding load vector. All mathematical operations (i.e., the linear combination in Equation (6) and the linear solve in Equation (7)) are recorded in the computational graph through Pytorch autograd (Paszke et al., 2017). The predicted surface deflections at geophone locations are extracted by index-selecting at the corresponding sensor nodes.

The inversion seeks the modulus vector  $\mathbf{E} = [E_1, E_2, \dots, E_i]^\top$  that minimizes the mean squared error between the predicted and observed surface displacements:

$$\mathcal{L}_{\text{data}}(\mathbf{E}) = \frac{1}{m} \sum_{j=1}^m \left\| \hat{\mathbf{u}}_j - \mathbf{u}_j^{\text{obs}} \right\|^2 \quad (8)$$

where  $m$  is the number of sensor nodes,  $\hat{\mathbf{u}}_j \in \mathbb{R}^2$  is the predicted displacement vector at sensor node  $j$ , and  $\mathbf{u}_j^{\text{obs}}$  is the corresponding observation. The gradient  $\nabla_{\mathbf{E}} \mathcal{L}_{\text{data}}$  is obtained via a reverse-mode AD backward pass, yielding sensitivities with respect to all moduli. The resulting gradient is then used by the optimizer to update  $\mathbf{E}$ .

## 3.2. Physics-Informed Neural Network (PINN)

### 3.2.1. Vanilla PINN

In the vanilla PINN, a single fully connected network  $\mathcal{N}_\theta : (r, z) \mapsto (u_r, u_z)$  is trained to predict the displacement field everywhere in the domain. The network architecture consists of an input

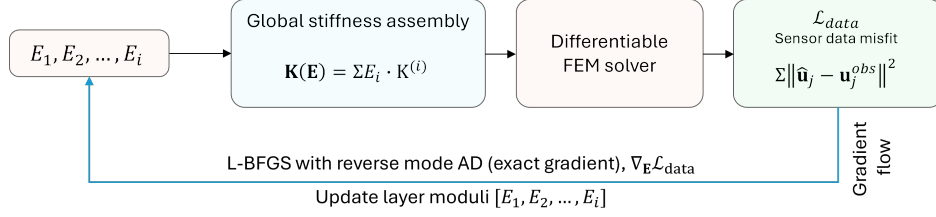


Figure 2: Computational flow of the DiffFEM inversion framework. The layer moduli  $\mathbf{E}$  enter through the global stiffness assembly, the linear system is solved by a differentiable FEM solver, and the data misfit loss  $\mathcal{L}_{\text{data}}$  is evaluated at sensor locations. Exact gradients are propagated back to  $\mathbf{E}$  via reverse-mode AD (blue arrow).

layer (2 neurons), three hidden layers (64 neurons each), and an output layer (2 neurons), with the hyperbolic tangent activation function applied at all hidden layers.

In standard PINN training, boundary conditions are typically imposed as penalty terms in the loss function (Raissi et al., 2019), introducing additional weights that complicate loss balancing. To avoid this issue, we enforce the essential boundary conditions as hard constraints by multiplying the network output by trial functions that vanish at the constrained boundaries (Sukumar and Srivastava, 2022). This construction satisfies the boundary conditions exactly without an additional penalty term in the loss. Specifically, the predicted displacements are constructed as:

$$\hat{u}_r(r, z) = r(L - r)z \mathcal{N}_\theta^{(r)}(r, z), \quad (9)$$

$$\hat{u}_z(r, z) = z \mathcal{N}_\theta^{(z)}(r, z), \quad (10)$$

where  $L$  is the domain width, and  $\mathcal{N}_\theta^{(r)}$ ,  $\mathcal{N}_\theta^{(z)}$  are the radial and vertical output components of the network, respectively. This construction exactly satisfies  $\hat{u}_r = 0$  at  $r = 0$  (axisymmetry),  $r = L$  (far-field boundary), and  $z = 0$  (rigid base), and  $\hat{u}_z = 0$  at  $z = 0$ , without requiring penalty terms.

The total loss combines a physics residual and a data misfit term:

$$\mathcal{L} = \lambda_{\text{phy}} \mathcal{L}_{\text{phy}} + \lambda_{\text{data}} \mathcal{L}_{\text{data}}, \quad (11)$$

where the physics loss enforces nodal equilibrium using the assembled FEM stiffness matrix:

$$\mathcal{L}_{\text{phy}} = \frac{1}{|\mathcal{I}_f|} \sum_{i \in \mathcal{I}_f} \|\mathbf{K}(\mathbf{E}) \hat{\mathbf{u}} - \mathbf{F}\|_i^2, \quad (12)$$

with  $\mathcal{I}_f$  denoting the set of free degree-of-freedom indices. The data loss  $\mathcal{L}_{\text{data}}$  is identical in form to Eq. (8). PINN treats both elastic moduli  $\mathbf{E}$  and  $\theta$  as trainable parameters, so AD computes the  $\nabla_{\mathbf{E}}\mathcal{L}$  and  $\nabla_{\theta}\mathcal{L}$  and the results are passed to a gradient-based optimization algorithm to jointly updates  $\mathbf{E}$  and  $\theta$ .

This single network-based PINN architectures typically face convergence challenges for systems with discontinuous domains (Jagtap and Karniadakis, 2020; Peng and Panesar, 2025), such as pavement systems, where the layer’s modulus sharply changes.

### 3.2.2. Extended PINN with domain decomposition (XPINN)

To address the convergence failure of vanilla PINN under sharp modulus discontinuities at layer interfaces (detailed in Section 4), an extended PINN with domain decomposition (XPINN) (Jagtap and Karniadakis, 2020) is adopted in which each pavement layer is assigned a dedicated sub-network. Figure 3 shows the overview. For the three-layer system, three independent networks  $\mathcal{N}_{\theta_1}$ ,  $\mathcal{N}_{\theta_2}$ , ...,  $\mathcal{N}_{\theta_i}$  share the same architecture as described in the vanilla PINN section (i.e., three hidden layers with the width of 64 neurons), corresponding to the surface course, base, and subgrade, respectively.

The composite displacement field is defined piecewise by domain, with each sub-network active exclusively within its assigned layer domain  $\Omega_i$ .

$$\hat{\mathbf{u}}(r, z) = \begin{cases} \mathcal{N}_{\theta_1}(r, z), & z \in \Omega_1, \\ \mathcal{N}_{\theta_2}(r, z), & z \in \Omega_2, \\ \vdots & \vdots \\ \mathcal{N}_{\theta_i}(r, z), & z \in \Omega_i \end{cases} \quad (13)$$

where  $\Omega_i$  denotes the subdomain of layer  $i$ ,  $\mathcal{N}_{\theta_i}$  is the neural network associated with that layer  $i$ . Boundary conditions are applied to the composite field using the same trial functions as

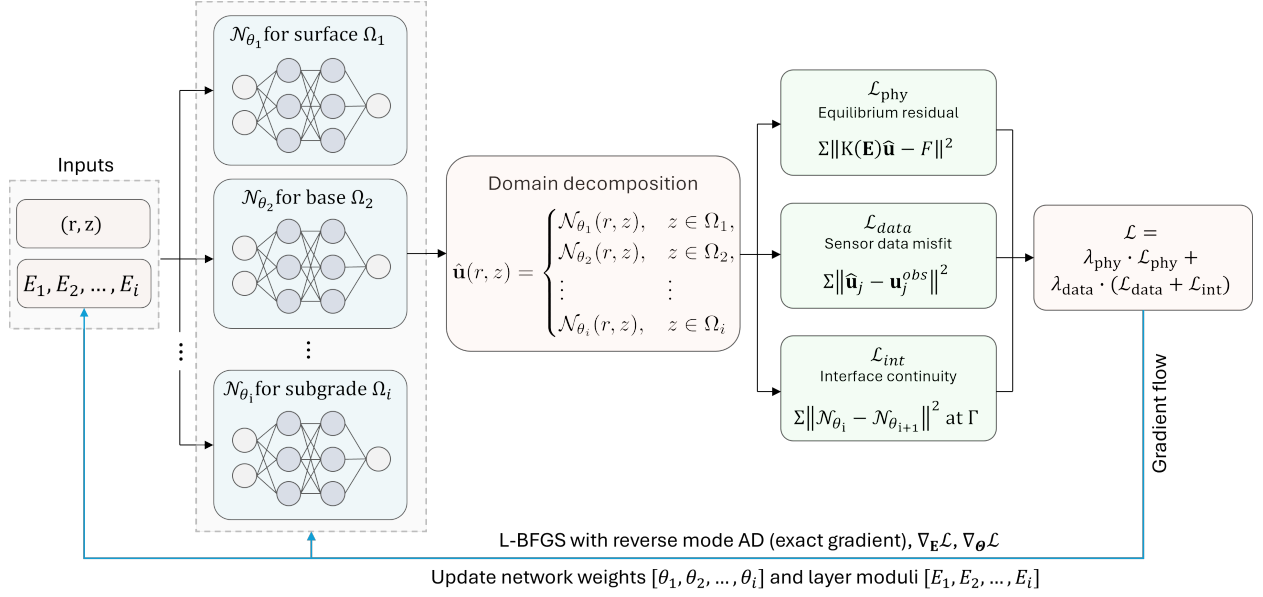


Figure 3: Architecture of the XPINN inversion framework. Three independent sub-networks  $\mathcal{N}_{\theta_1}$ ,  $\mathcal{N}_{\theta_2}$ ,  $\mathcal{N}_{\theta_3}$  approximate the displacement field in the surface, base, and subgrade domains, respectively. The total loss combines a physics residual  $\mathcal{L}_{\text{phy}}$ , a sensor (i.e., geophone) data misfit  $\mathcal{L}_{\text{data}}$ , and an interface continuity penalty  $\mathcal{L}_{\text{int}}$ . The layer moduli  $\mathbf{E}$  and all network weights are updated jointly via reverse-mode AD (blue arrows).

in Equation (9)-(10).

Displacement continuity at the layer interfaces is enforced as soft constraints appended to the data loss:

$$\mathcal{L}_{\text{int}} = \sum_{i=1}^{N_i-1} \frac{1}{|\Gamma_{i,i+1}|} \sum_{j \in \Gamma_{i,i+1}} \|\mathcal{N}_{\theta_i}(\mathbf{x}_j) - \mathcal{N}_{\theta_{i+1}}(\mathbf{x}_j)\|^2 \quad (14)$$

where  $\Gamma_{i,i+1}$  denotes the set of mesh nodes lying on the interface between layers  $i$  and  $i+1$ . The data loss in Equation (11) is combined with  $\mathcal{L}_{\text{int}}$ , so that the total optimization objective becomes:

$$\mathcal{L}_{\text{XPINN}} = \lambda_{\text{phy}} \mathcal{L}_{\text{phy}} + \lambda_{\text{data}} (\mathcal{L}_{\text{data}} + \mathcal{L}_{\text{int}}) \quad (15)$$

XPINN treats  $\mathbf{E}$  and three network parameter sets  $\Theta = \{\theta_1, \theta_2, \dots, \theta_i\}$  as trainable parameters. Accordingly, AD computes  $\nabla_{\mathbf{E}}\mathcal{L}$  and  $\nabla_{\Theta}\mathcal{L}$ , and the gradient-based optimization updates the parameters jointly. Loss weights are set to  $\lambda_{\text{phy}} = 1$  and  $\lambda_{\text{data}} = 10^3$  following the sensitivity study discussed in Section 4.

### 3.3. DiffFEM vs. PINN

Table 1 summarizes the structural differences between DiffFEM and XPINN. The key distinction is that DiffFEM satisfies the governing equations exactly at every iteration: the linear system in Equation (7) is solved to machine precision. By contrast, XPINN enforces equilibrium only approximately through the soft physics loss  $\mathcal{L}_{\text{phy}}$ . Consequently, DiffFEM optimizes only the three layer moduli, whereas XPINN jointly optimizes the moduli and all network weights across three sub-networks, which is about 26,000 parameters counts.

Table 1: Structural comparison of DiffFEM and XPINN.

Item	DiffFEM	XPINN
Physics enforcement	Exact (FEM formulation)	Soft (loss term)
Free parameters	Moduli	Moduli + network weights
Interface continuity	Exact (shared mesh nodes)	Soft (loss term)
Loss terms	Data only	Weighted joint loss with physics + data

### 3.4. Optimization setting

The gradient-based optimizer used for both DiffFEM and XPINN is the limited-memory Broyden–Fletcher–Goldfarb–Shanno (L-BFGS) algorithm (Liu and Nocedal, 1989), a quasi-Newton method that uses gradient information to construct a limited-memory approximation of the inverse Hessian and thereby exploit local curvature of the loss function. We use L-BFGS rather than a first-order optimizer such as Adam since curvature-informed updates can provide faster convergence and lower residuals in PINN-type optimization problems than purely first-order updates (Rathore et al., 2024). We initialize the moduli to  $\mathbf{E} = 0.1$  MPa, a value deliberately set well below the expected layer stiffnesses to provide an unbiased assessment of convergence behavior for both methods. Network weights in XPINN are initialized using Xavier uniform initialization (Kumar, 2017). Convergence is assessed by manually monitoring the loss trajectory and the evolution of the three inferred moduli with iteration count. We terminate the optimization when both the loss and the modulus estimates cease to exhibit systematic change, indicating that the optimizer reaches a stationary point.

### 3.5. Synthetic benchmark setup

Figure 4 illustrates the finite element setup. A uniformly distributed vertical load is applied over a circular plate of radius  $a = 0.15$  m at the pavement surface. The total applied load is approximately 49.5 kN, corresponding to a contact pressure of 0.7 MPa. The pavement is modeled as a three-layer axisymmetric domain with radial extent  $r \in [0, 1.5]$  m and depth  $z \in [0, 1.5]$  m, where  $z = 1.5$  m denotes the pavement surface and  $z = 0$  m denotes the base of the subgrade. Both the radial and vertical extents are set to five times the loading diameter to minimize boundary effects, following the recommendation of (Kuo and Chou, 2004). The layer configuration and reference elastic properties used to generate the synthetic FWD data are listed in Table 2; these material properties are adopted from (Tarefder and Ahmed, 2014). The domain is discretized using 4-node bilinear quadrilateral elements, resulting in a mesh with 78 nodes in the radial direction and 76 nodes in the vertical direction, for a total of 5,928 nodes and 5,775 elements.

Table 2: Layer configuration and reference material properties.

Layer	Depth range	Thickness	$E$ (MPa)	$\nu$
Surface (AC)	$1.40 \leq z \leq 1.50$ m	100 mm	1,378	0.35
Base course	$1.15 \leq z < 1.40$ m	250 mm	206	0.35
Subgrade	$0.00 \leq z < 1.15$ m	1,150 mm	69	0.35

Ten geophone sensors are located at the pavement surface ( $z = 1.5$  m) at 0.15 m intervals from  $r = 0$  to  $r = 1.35$  m, providing displacement observations  $\mathbf{u}$ . To evaluate robustness to measurement uncertainty, six noise cases are considered, corresponding to noise standard deviations of  $\sigma_n \in \{0, 1, 2, 3, 4, 5\}$   $\mu\text{m}$ . Here,  $\sigma_n = 0$  represents the noise-free case, while the remaining five cases are generated by adding independent zero-mean Gaussian noise to the displacement at all sensor locations. This range is selected based on typical systematic FWD measurement errors ( $\pm 2$   $\mu\text{m}$ ) reported in (Smith et al., 2017). For each noise level, the noisy dataset is generated offline prior to inversion and then kept fixed across all methods, so that any performance differences can be attributed solely to the inversion algorithm rather than to stochastic variation in the input data. Figure 5 illustrates the resulting surface deflection basins for the noise-free case and for two representative noisy cases,  $\sigma_n = 1$   $\mu\text{m}$  and  $\sigma_n = 5$   $\mu\text{m}$ . The bottom row shows the residuals

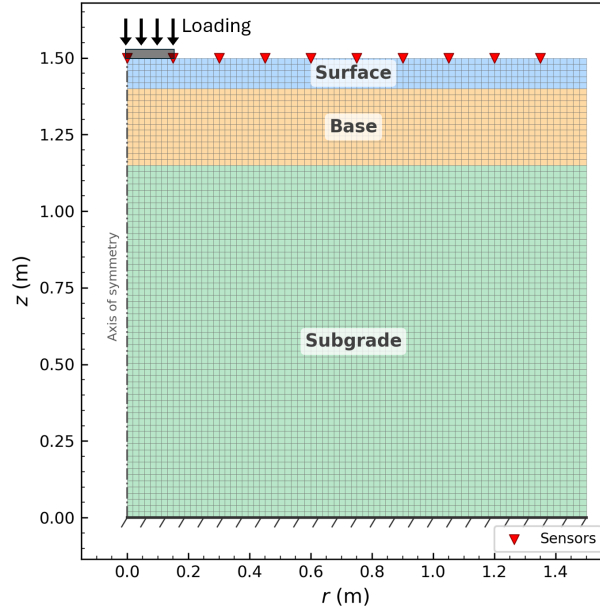


Figure 4: Axisymmetric finite element domain for the three-layer pavement system. The mesh spans  $r \in [0, 1.5]$  m and  $z \in [0, 1.5]$  m, with refinement near the loaded zone. Ten geophone sensors (red triangles) are placed at the pavement surface at 0.15 m intervals.

between noisy and noise-free responses, with dashed lines indicating the  $\pm\sigma_n$  bounds.

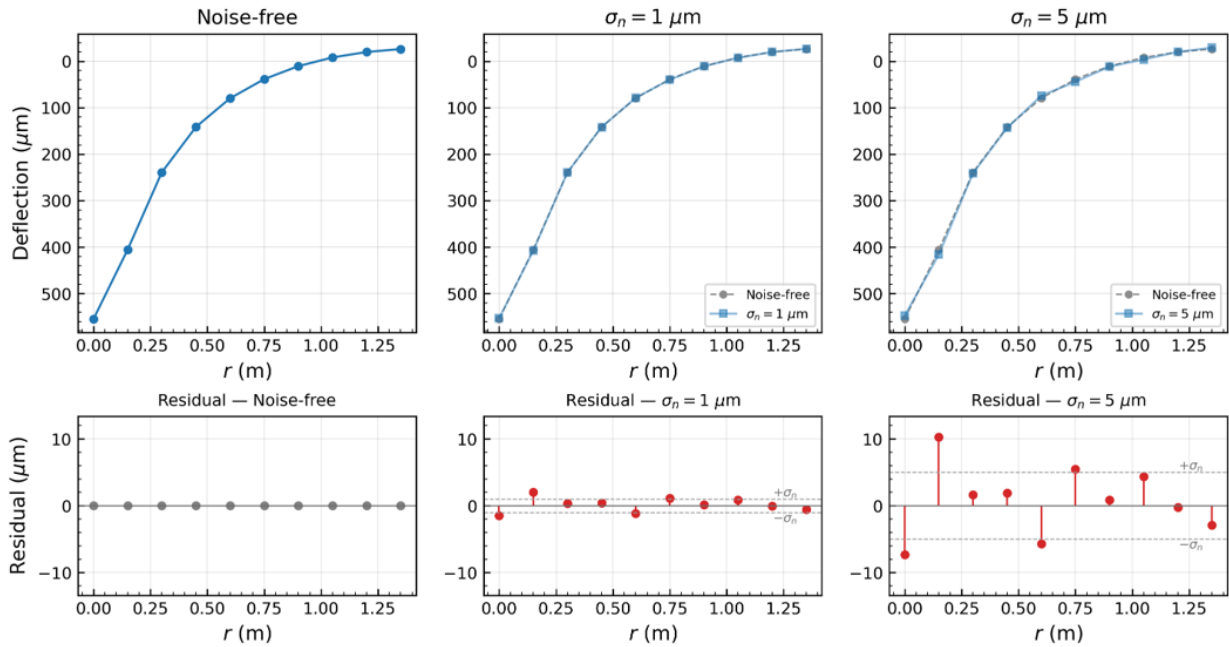


Figure 5: Surface deflection basins measured by FWD geophone sensors under three noise conditions: noise-free,  $\sigma_n = 1 \mu\text{m}$ , and  $\sigma_n = 5 \mu\text{m}$ . Top row: deflection versus radial distance from the load center. Bottom row: residuals (noisy – noise-free) at each sensor location; dashed lines indicate the  $\pm\sigma_n$  bounds.

## 4. Results

This section presents the inversion results for both DiffFEM and XPINN following the synthetic benchmark setup described in Section 3.5.

### 4.1. Noise-free inversion

We first evaluate both DiffFEM and XPINN using noise-free measurements to isolate their intrinsic algorithmic behavior from measurement uncertainty. For XPINN, we adopt loss weights  $\lambda_{\text{phy}} = 1$ ,  $\lambda_{\text{data}} = 10^3$  and a sub-network architecture of  $L = 3$  hidden layers with  $H = 64$  neurons, as explained in method section (Section 3). Figure 6 compares the optimization histories of the two approaches. DiffFEM (Figure 6b) converges within approximately 40 iterations, reducing the data loss below  $10^{-17}$  and recovering the three elastic moduli with relative errors on the order of  $\mathcal{O}(10^{-9})$ – $\mathcal{O}(10^{-10})$  compared to the ground-truth values listed in Table 2.

In contrast, XPINN (Figure 6a) requires roughly  $4 \times 10^5$  iterations to reach convergence. Its data loss plateaus near  $10^{-8}$ , while the physics residual  $\mathcal{L}_{\text{phy}}$  stagnates around  $10^{-4}$ . Although XPINN estimates moduli that are reasonably close to the true values, the relative errors, -1.1%, +1.0%, and -6.9% for the surface, base, and subgrade layers, respectively, remain several orders of magnitude larger than those obtained with DiffFEM. This discrepancy can be attributed to the fundamentally different treatments of the governing equations: XPINN enforces the physics as a soft penalty term in the loss function (Equation (15)), which does not strictly guarantee satisfaction of the equations, whereas DiffFEM imposes them as hard constraints through the finite element solver.

These discrepancies in the recovered moduli propagate to the predicted displacement fields, as shown in Figure 7. DiffFEM accurately reproduces both  $u_r$  and  $u_z$  across the entire domain, with negligible error. XPINN captures the overall displacement patterns but exhibits localized error concentrations: the error in  $u_r$  increases below the base-subgrade interface, while the error in  $u_z$  is concentrated along the subgrade centerline.

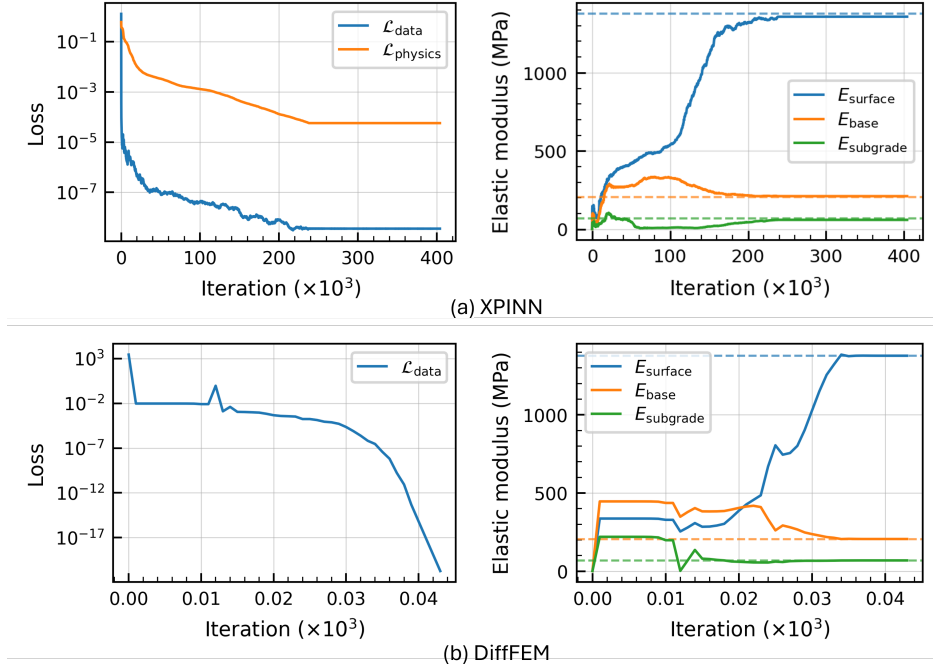


Figure 6: Convergence histories for the noise-free inversion. Top row: XPINN loss components (left) and inferred elastic moduli (right) over  $400 \times 10^3$  iterations. Bottom row: DiffFEM data loss (left) and inferred moduli (right) over fewer than 60 iterations. Dashed horizontal lines indicate the ground-truth moduli.

#### 4.1.1. Limitations and hyperparameter sensitivity of PINN-based inverse analysis

The XPINN formulation used in the previous comparison was not the first architecture considered. As a preliminary study, we also evaluated the vanilla PINN described in Section 3.2. However, the vanilla PINN failed to recover the layer moduli, as illustrated in Figure 8. Specifically, all layer moduli converged to arbitrary values, even in the absence of measurement noise. This failure is consistent with the well-documented limitations of standard PINNs for discontinuous or multi-domain systems (Jagtap and Karniadakis, 2020; Peng and Panesar, 2025). Sharp modulus contrasts at layer interfaces induce slope discontinuities in the displacement field, introducing high-frequency components that a single global network struggles to represent efficiently due to spectral bias (Naser, 2025; Peng and Panesar, 2025). In smooth systems, vanilla PINN may still work well under the noisy conditions (Gong et al., 2025; Moon et al., 2025). However, since our problem, multi-layered pavement systems, has strictly discontinuous modulus changes, the spectral bias issue is expected to be inevitable with standard PINN. Accordingly, we exclude

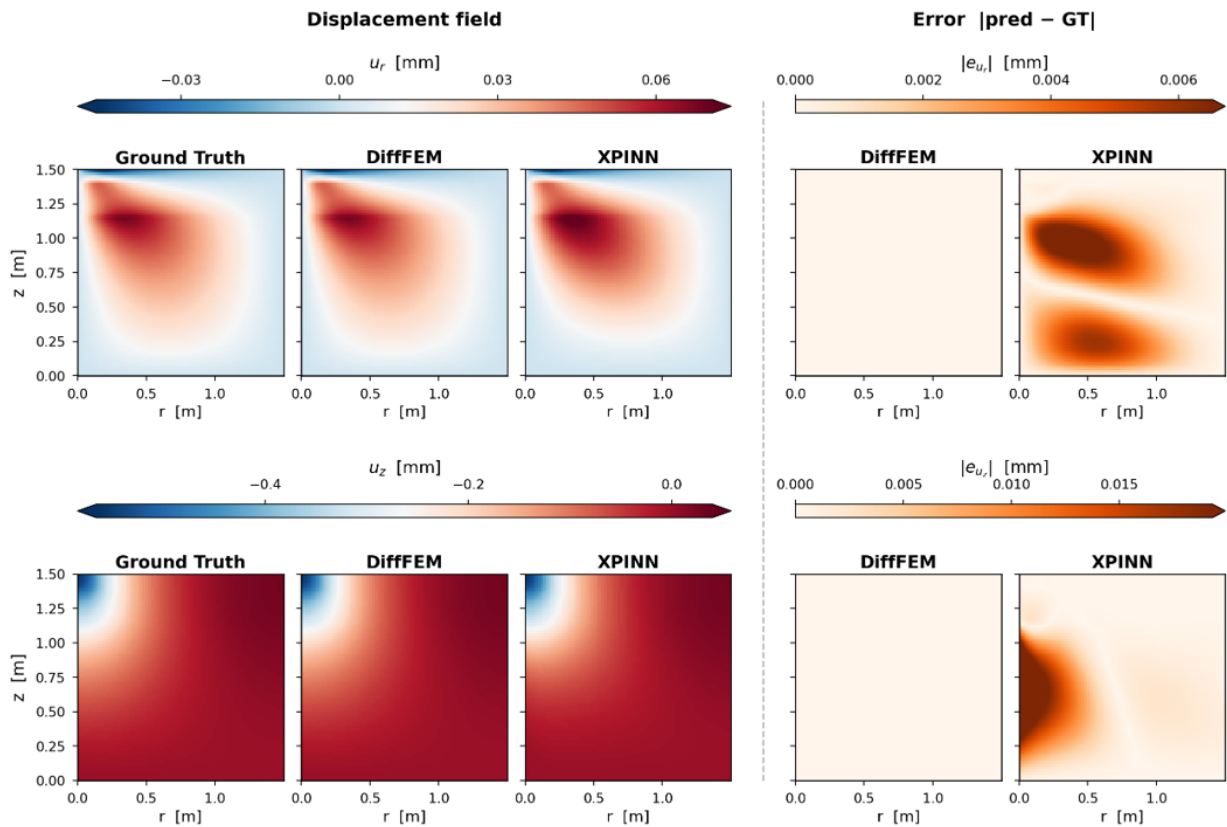


Figure 7: Predicted displacement fields and pointwise errors for the noise-free case. Left columns: ground-truth (GT), DiffFEM, and XPINN predictions for radial ( $u_r$ , top) and vertical ( $u_z$ , bottom) displacements. Right columns: absolute error  $|pred - GT|$  for DiffFEM and XPINN.

Table 3: XPINN loss-weight sweep on the noise-free benchmark (network fixed at  $L=3$  hidden layers,  $H=32$  units;  $\lambda_{\text{phys}}=1$ ). Recovered layer moduli (MPa) and signed relative errors (%) versus the true values listed in Table 2.

$\lambda_{\text{data}}/\lambda_{\text{phys}}$	Recovered modulus (MPa)			Relative error (%)		
	$E_{\text{surface}}$	$E_{\text{base}}$	$E_{\text{subgrade}}$	$E_{\text{surface}}$	$E_{\text{base}}$	$E_{\text{subgrade}}$
$10^0$	-2936	-44	-1	-313.1	-121.5	-102.2
$10^1$	318	289	114	-76.9	+40.2	+65.5
$10^2$	1454	188	81	+5.5	-8.6	+17.2
$10^3$	1358	210	59	-1.4	+2.1	-14.4

the vanilla PINN from further consideration and focus the sensitivity analysis in this section on the XPINN-based results.

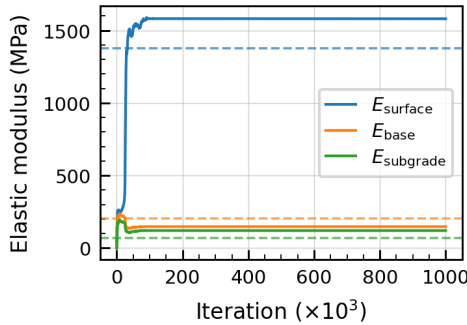


Figure 8: Modulus convergence history for the vanilla PINN formulation without noise. Dashed horizontal lines indicate the true moduli.

The composite XPINN objective (Equation (15)) consists of a physics residual term and a data misfit term. We first investigate the sensitivity to the loss-weight ratio  $\lambda_{\text{data}}/\lambda_{\text{phys}}$  in recovering the true moduli. Table 3 summarizes the results of a parameter sweep with the network architecture fixed at  $L=3$  hidden layers and  $H=32$  neurons per layer. When  $\lambda_{\text{data}}/\lambda_{\text{phys}} = 1$ , XPINN fails, producing errors exceeding 100% in all layers. As the ratio increases, the accuracy improves. Only when  $\lambda_{\text{data}}/\lambda_{\text{phys}} = 10^3$  do the surface and base moduli converge to within approximately 1-2% of the ground truth; however, the subgrade modulus still exhibits a substantial relative error of  $-14.4\%$ . These results highlight the dependence of PINN performance on loss-weight tuning, a known challenge in PINN-based inverse analysis (Chou et al., 2025; Faroughi et al., 2024). Adaptive loss-weighting schemes (Wang et al., 2021; McClenny and Braga-Neto, 2023) aim to mitigate this issue, but they typically introduce algorithmic design choices and computational overhead.

Table 4: XPINN network-size sweep on the noise-free benchmark (loss weights fixed at  $\lambda_{\text{data}}=10^3$ ,  $\lambda_{\text{phys}}=1$ ). Recovered layer moduli (MPa) and signed relative errors (%) for hidden-layer counts  $L \in \{2, 3, 4\}$  and per-layer widths  $H \in \{16, 32, 64, 128\}$ , against true values listed in Table 2.

$L$	$H$	Recovered modulus (MPa)			Relative error (%)		
		$E_{\text{surface}}$	$E_{\text{base}}$	$E_{\text{subgrade}}$	$E_{\text{surface}}$	$E_{\text{base}}$	$E_{\text{subgrade}}$
2	16	1303	211	61	-5.5	+2.5	-12.0
	32	1374	202	71	-0.3	-1.9	+3.4
	64	1254	221	40	-9.0	+7.4	-42.6
	128	1361	208	63	-1.2	+0.8	-8.2
3	16	1499	173	118	+8.8	-16.2	+70.9
	32	1358	210	59	-1.4	+2.1	-14.4
	64	1363	208	64	-1.1	+1.0	-6.9
	128	1385	202	69	+0.5	-1.9	-0.6
4	16	1541	171	22	+11.8	-17.1	-68.8
	32	1368	208	61	-0.8	+1.2	-12.3
	64	1365	207	64	-0.9	+0.3	-6.8
	128	1375	207	62	-0.3	+0.5	-10.6

Even after selecting the best-performing loss weights, a second challenge emerges: sensitivity to network architecture. Table 4 presents results obtained using the optimal loss-weight ratio ( $\lambda_{\text{data}}/\lambda_{\text{phys}} = 10^3$ ) across various architectures with hidden-layer counts  $L \in \{2, 3, 4\}$  and widths  $H \in \{16, 32, 64, 128\}$ . The surface modulus is relatively robust, with most configurations yielding errors within a few percent. The base modulus shows moderate sensitivity, with errors typically ranging from 1% to 17%. In contrast, the subgrade modulus exhibits substantial variability, ranging from  $-68.8\%$  at  $(L=4, H=16)$  to  $+70.9\%$  at  $(L=3, H=16)$ , without a clear trend with respect to network depth or width. This likely reflects the low sensitivity of surface deflections to the subgrade modulus, which yields weak gradients that the optimizer cannot reliably follow toward the true value. Notably, this architectural sensitivity underscores that the computational effort required for hyperparameter tuning is a prerequisite for achieving PINN’s successful convergence.

Overall, these results demonstrate that XPINN-based inverse analysis requires careful and problem-specific tuning of both loss weights and network architecture. Even under noise-free conditions, the method exhibits significant variability in performance, deeper layers as well, which complicates its practical deployment.

## 4.2. Noisy inversion

We next evaluate both methods in the presence of measurement noise, using the same hyperparameters as in the noise-free case for both DiffFEM and XPINN. The cases of  $\sigma_n = 1 \mu\text{m}$  and  $\sigma_n = 5 \mu\text{m}$  are examined in detail, while the full set of results is summarized in Section 4.2.3 with their quantitative values shown in Table A.5 in Appendix section.

### 4.2.1. Low noise ( $\sigma_n = 1 \mu\text{m}$ )

Figure 9 presents the optimization histories for the case  $\sigma_n = 1 \mu\text{m}$ . DiffFEM (Figure 9b) again converges rapidly, after approximately 40 iterations. The data loss plateaus below  $10^{-5}$ , and the recovered moduli remain within a few percent of the true values. Specifically, the relative errors are 2.7%, 1.2%, and 0.05% for the surface, base, and subgrade layers, respectively. Among the three layers, the surface modulus exhibits the largest relative error.

In contrast, XPINN (Figure 9a) fails to recover the correct moduli. Although the data loss reaches a very low plateau (approximately  $10^{-6}$ ), the physics residual stagnates at approximately  $10^{-3}$ . The estimated surface and base moduli converge to nearly identical wrong values of about 350 MPa, while the subgrade modulus collapses toward zero, resulting in relative errors of 74%, 67%, and 94%, respectively. The combination of low data loss and non-negligible physics residual indicates that the recovered displacement field fits well with the sensor observations without satisfying global equilibrium—a solution admissible only under the soft enforcement of the governing equations, which is what PINNs do. The resulting displacement and error fields in Figure 10 corroborate this interpretation, showing substantial deviations from the ground-truth displacement field throughout the domain. This behavior suggests that the XPINN failure is not simply a noise-induced perturbation of the inverse solution, but an optimization failure in which the network finds a low data loss displacement field that is not consistent with the correct material parameters. On the other hand, DiffFEM shows very accurate displacement fields Figure 10 due to the successful modulus recovery.

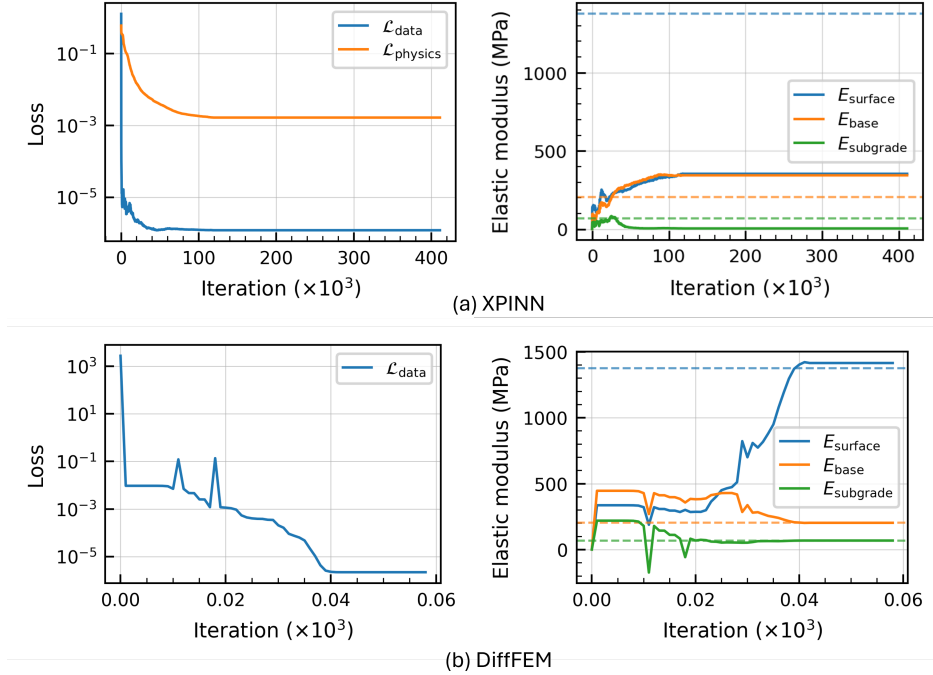


Figure 9: Convergence histories for the noisy inversion with  $\sigma_n = 1 \mu\text{m}$ . Top row: XPINN loss components and inferred moduli. Bottom row: DiffFEM loss and inferred moduli. Dashed horizontal lines indicate the ground-truth moduli.

#### 4.2.2. High noise ( $\sigma_n = 5 \mu\text{m}$ )

Under high noise, DiffFEM (Figure 11b) still shows fast convergence, with the data loss plateau rising to  $\sim 10^{-3}$ . The recovered moduli drift from the ground truth (14%, 6.2%, and 0.09% for the surface, base, and subgrade) due to the measurement noise, but the result remains reasonable. The subgrade is still recovered to sub-percent accuracy. XPINN (Figure 11a) fails to identify the moduli, more severely than the case with  $\sigma_n = 1 \mu\text{m}$ . The base modulus drifts monotonically upward throughout training and reaches roughly 1,000 MPa, nearly five times the true values, while the surface and subgrade estimates remain well below their true values shown in Table 2. Figure 12 illustrates the consequence for the reconstructed displacement field. DiffFEM tracks the ground truth with small errors throughout the domain for both  $u_r$  and  $u_z$ . The XPINN's displacement fields show a physically incorrect pattern near the loaded zone and also along the centerline below the base layer.

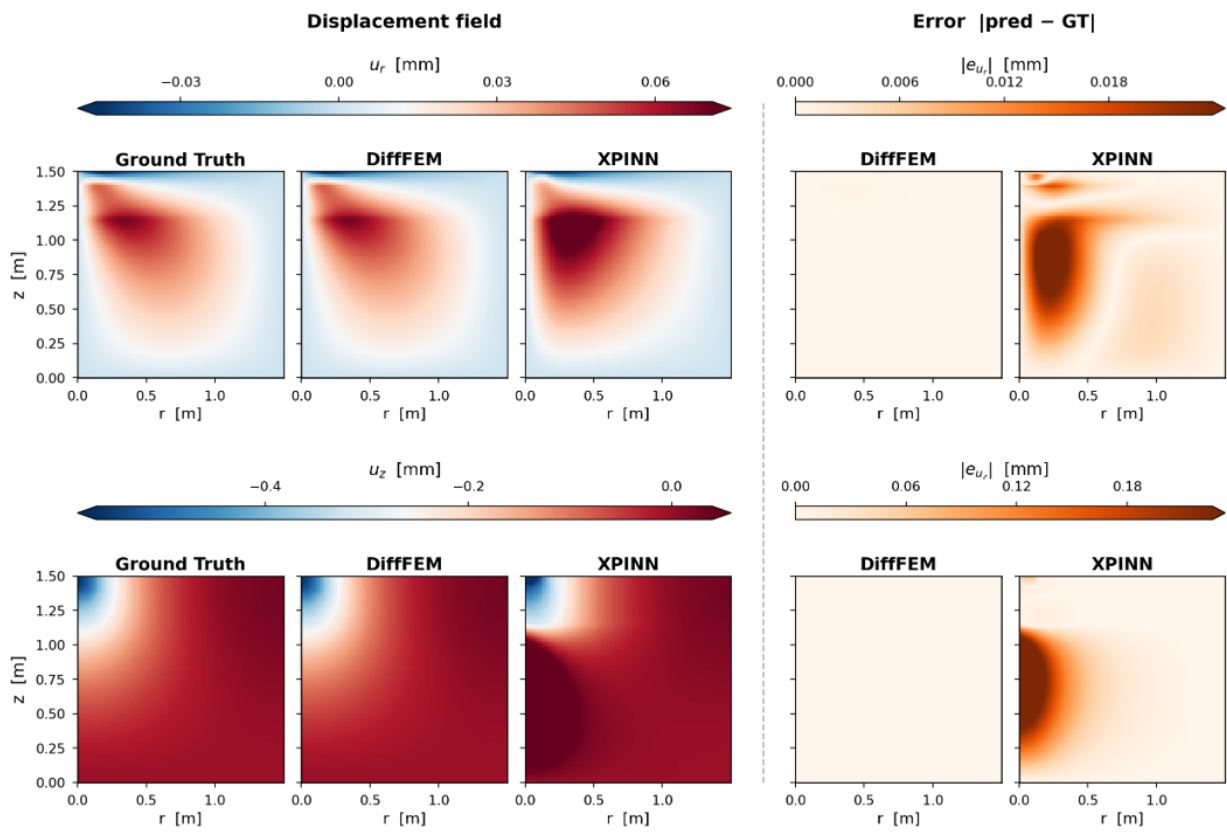


Figure 10: Predicted displacement fields and pointwise errors for  $\sigma_n = 1 \mu\text{m}$ . The plot layout follows that of Figure 7.

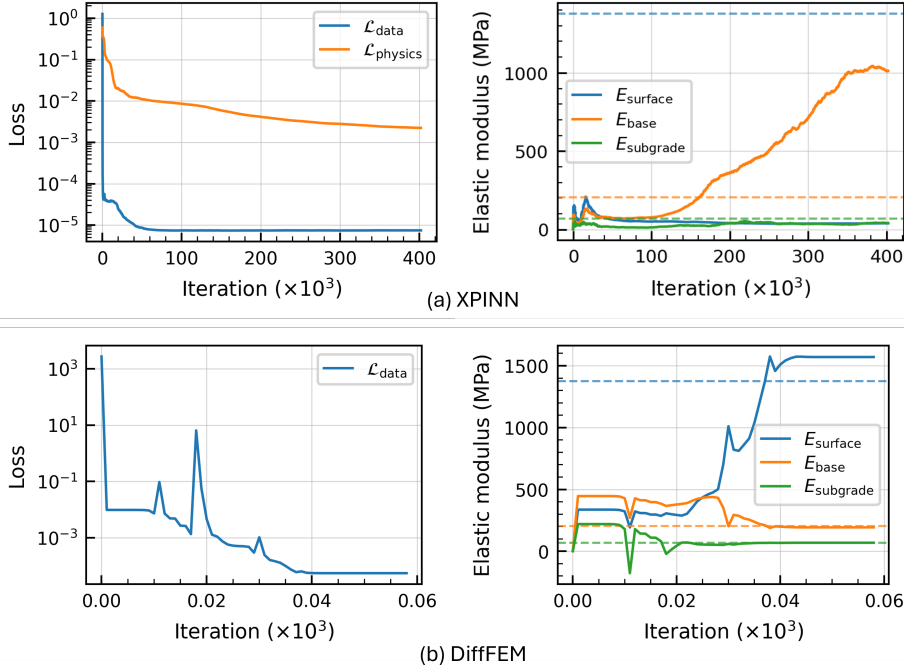


Figure 11: Convergence histories for the noisy inversion with  $\sigma_n = 5 \mu\text{m}$ . Top row: XPINN loss components and inferred moduli. Bottom row: DiffFEM loss and inferred moduli. Dashed horizontal lines indicate the ground-truth moduli.

#### 4.2.3. Summary across noise levels

Figure 13 summarizes the performance of both methods across all tested noise levels, with quantitative values reported in Table A.5. DiffFEM degrades gracefully with increasing noise: the displacement RMSE grows approximately linearly with  $\sigma_n$ , and the modulus errors remain bounded, reaching at most 14.0% (surface), 6.2% (base), and 0.11% (subgrade) at  $\sigma_n = 5 \mu\text{m}$ . XPINN, in contrast, exhibits a displacement RMSE about an order of magnitude larger than that of DiffFEM, indicating that XPINN’s accuracy is limited by optimization-related errors rather than by measurement noise. Its modulus errors are correspondingly large and erratic for  $\sigma_n \geq 1 \mu\text{m}$ , with base errors reaching up to 391% and the dominant failure mode shifting with noise level—from surface-base collapse at low noise to severe base overestimation at high noise. A notable feature of DiffFEM is that the subgrade modulus is recovered to within 0.2% under all tested conditions.

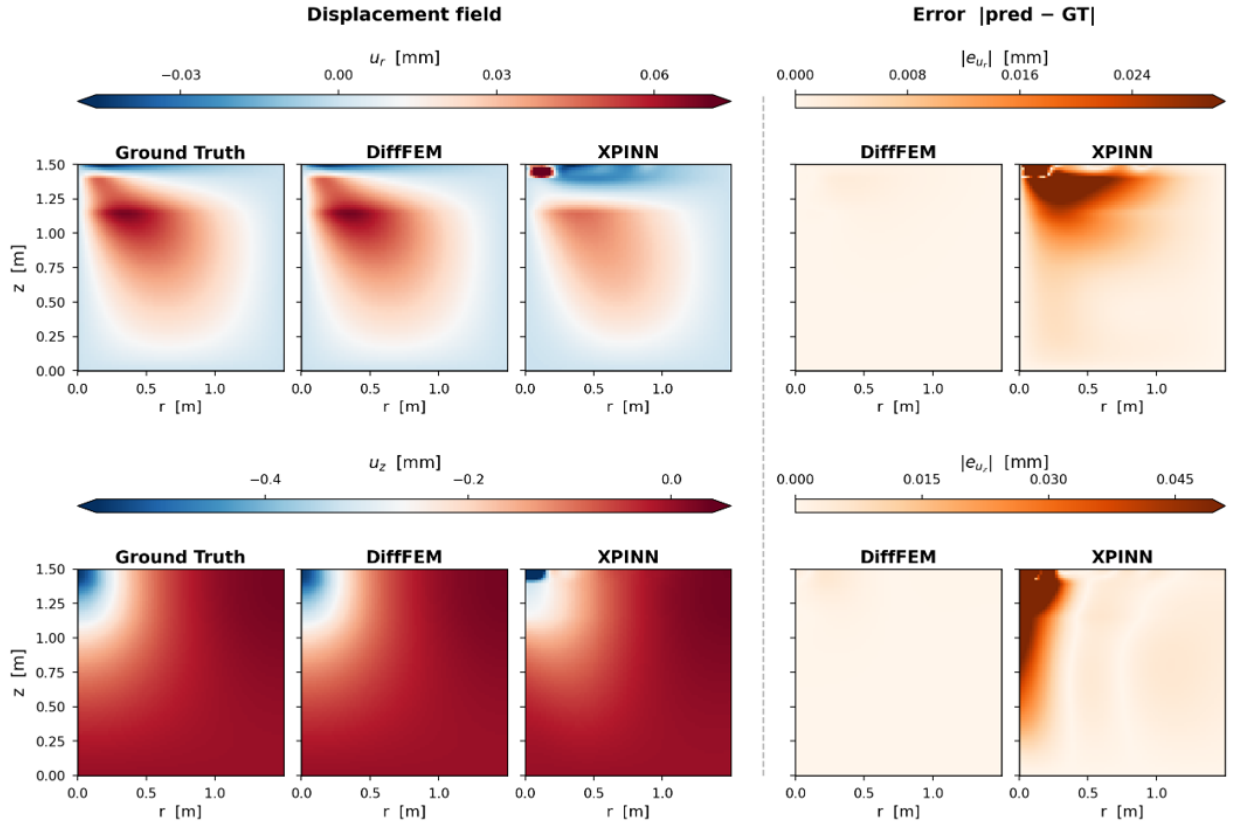


Figure 12: Predicted displacement fields and pointwise errors for  $\sigma_n = 5 \mu\text{m}$ . The plot layout follows that of Figure 7.

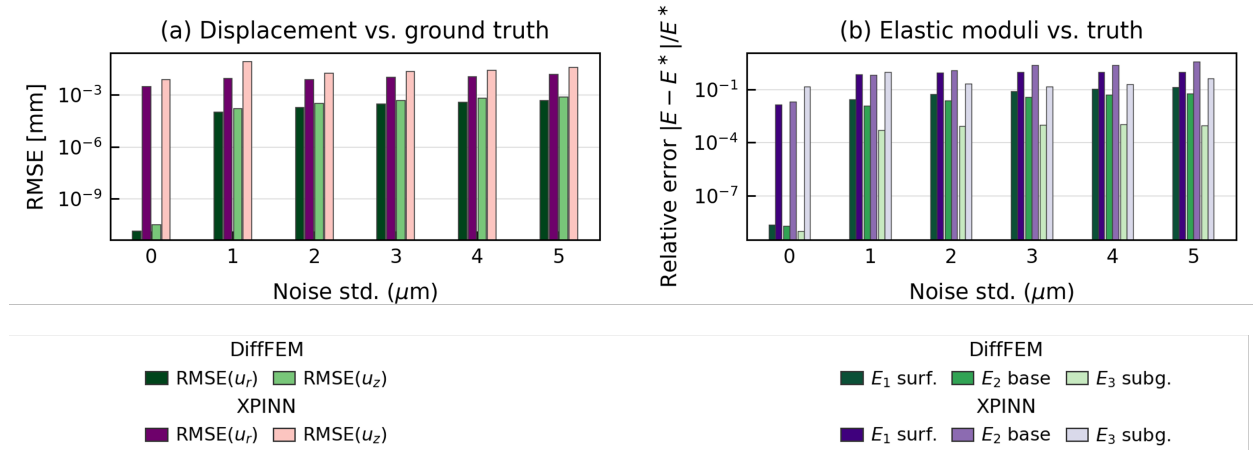


Figure 13: Summary of inversion accuracy across all noise levels ( $\sigma_n = 0\text{--}5 \mu\text{m}$ ). (a) Root-mean-square error of the predicted surface displacements relative to the ground-truth solution. (b) Relative error of the inferred elastic moduli for each layer. All axes are logarithmic.

### 4.3. Computational cost

We compare the computational efficiency of DiffFEM and XPINN on the noise-free inversion shown in Figure 6, using a NVIDIA RTX 5090 GPU. DiffFEM completes the full optimization iterations in approximately 60 s, whereas XPINN requires roughly 10 h to reach an approximate stationary point after  $400 \times 10^3$  iterations—more than two orders of magnitude slower. The GPU memory consumption is similar for both methods with about 4 GB usage.

## 5. Discussion

The results above consistently show that DiffFEM outperforms XPINN in accuracy, robustness, and computational efficiency for FWD backcalculation. This observation raises a practical question: why does DiffFEM perform reliably in this setting, and under what conditions should each approach be preferred?

The superior performance of DiffFEM in this study appears to stem from several features of its formulation. First, the governing equations are enforced directly through the forward solve at every iteration, whereas in XPINN, they are imposed only as soft constraints in the loss function and therefore need not be satisfied exactly. Second, DiffFEM optimizes only the three layer moduli, while XPINN must simultaneously optimize the moduli, tens of thousands of neural-network weights, and interface-continuity terms. In addition, the PINN loss is a composite objective, requiring the optimization process to balance multiple competing terms. This can make the loss landscape more complex and increase the likelihood of convergence to local optima (Rowan and Murphy-Blanchard, 2026). For this reason, previous studies have often adopted problem-specific architectural modifications and strategic adaptive optimization policy with second-order methods (Rathore et al., 2024; Moon et al., 2025). In the present setting, these factors make the PINN-based approaches challenging to train and can hinder reliable parameter identification in the presence of noisy data.

The practical advantage of DiffFEM, however, rests on an important prerequisite: the forward solver must be differentiable. In the present study, this requirement is straightforward to satisfy. Layered elastic theory under quasi-static loading reduces to a linear system (Equation (7)) that

is readily implemented within modern AD frameworks such as PyTorch. There are no adaptive mesh updates, and the constitutive model is linear elastic—features that simplify the use of AD in this setting. Many layered-elastic FWD backcalculation problems share these characteristics, which suggests that DiffFEM can be a strong option for this class of problems.

Not all forward solvers, however, can be made differentiable with equal ease. Contact algorithms involving non-smooth constraints, constitutive stress update with adaptive timestepping, and bifurcation problems with multiple solution branches can all present obstacles to AD-based differentiation: the gradient of the forward solution with respect to the material parameters can be undefined, discontinuous, or expensive to propagate through the computational graph. Making such solvers differentiable is an active area of research (Paulus et al., 2026), and in settings where a differentiable forward solver is difficult to construct, PINN-based approaches remain an attractive option. For example, PINNs have shown successful applications for contact problems (Sahin et al., 2024; Bai et al., 2025; Li et al., 2024) and elastoplastic constitutive update with return mapping (Eghbalian et al., 2023). In addition, PINNs can avoid an explicit linear solve and the need for a conforming finite element mesh in their classical form, where PINNs evaluate the particle differential equation residual by applying AD to the network output with respect to the input coordinates (Raissi et al., 2019). Therefore, observations at arbitrary sensor locations can be incorporated directly, while complex geometries or regions requiring higher local resolution can be addressed through targeted collocation-point sampling, although boundary-condition enforcement and sampling design remain important challenges (Cuomo et al., 2022).

We note, however, that the XPINN variant benchmarked in this study is not mesh-free in this sense. Its physics residual is assembled from precomputed FEM stiffness matrices (Equation (6)), so it inherits the mesh-generation and Degree of Freedom indexing machinery of DiffFEM while replacing only the linear solve with a neural parameterization of the displacement field. The mesh-free advantages above therefore apply to autograd particle differential equation residual PINNs (Raissi et al., 2019), not to the specific XPINN implementation compared here.

Beyond the residual formulation, the XPINN domain-decomposition strategy introduces its own scaling concern: each additional pavement layer requires a dedicated sub-network, and each

interior interface contributes a continuity penalty, so that both the total parameter count and the number of interface-matching terms grow linearly with the number of layers. DiffFEM, by contrast, scales more favorably, since adding a layer only introduces one additional unit stiffness matrix in the additive decomposition (Equation (6)) and one additional scalar modulus in the optimization, without altering the structure of the inverse problem or the linear system being solved.

A further consideration in DiffFEM is the memory footprint of reverse-mode AD. For problems involving long time integration, such as dynamic FWD analysis or viscoelastic pavement response, storing intermediate states for backpropagation can become memory-prohibitive. To mitigate this issue, DiffFEM may require specialized techniques such as gradient checkpointing (Choi and Kumar, 2024) to efficiently manage the memory. These complications do not arise in the quasi-static setting considered here. In such time-dependent extensions, PINNs are an appealing option, as they avoid unrolling a time-stepping computational graph. For instance, Hou et al. (2024) solved long-horizon forward and inverse problems efficiently without timestepping on wave propagation based on PINN.

Taken together, these observations suggest a practical guideline. When the forward solver is well established, numerically stable, and amenable to implementation within an AD framework—as in the layered-elastic FWD backcalculation problem studied here—DiffFEM appears to be a good starting option. In this setting, it imposes hard physics constraints that enforce equilibrium at every iteration through the forward solve, lets the optimization focus on system parameters without considering neural network surrogates, and converges in minutes rather than hours in the present benchmark. PINNs, while conceptually appealing for their ability to simultaneously solve the forward and inverse problems through soft physics constraints, should be applied with caution to problems of this type: the results of this study show that even with domain decomposition and careful hyperparameter tuning, the PINN formulation struggled to recover accurate modulus estimates under realistic noise conditions. PINNs may be more compelling in settings where FEM faces computational or numerical challenges in solving the governing equations, or when a differentiable forward solver is unavailable.

## 6. Conclusion

This study investigates recent AD-based inverse analysis approaches, PINN and DiffFEM, for backanalysis of pavement modulus from FWD tests. The results show that the suitability of these two approaches differs fundamentally for FWD backanalysis.

The standard PINN formulation does not recover the layer moduli due to the sharp material discontinuities inherent to layered pavements. Although XPINN with domain decomposition improves convergence in the noise-free case, its performance remains highly sensitive to the hyperparameter selection, including loss-weight selection and network architecture. Even after hyperparameter tuning, XPINN requires substantially more iterations and still produces suboptimal solutions because of the inherent formulation of PINNs, where governing equations and interface continuity are imposed only as soft constraints.

On the other hand, DiffFEM provides consistently more accurate and robust inversion results than XPINN. In the noise-free case, it recovers the target moduli to numerical precision. Under all tested noise levels, it remained stable and degraded gradually with increasing noise, while maintaining substantially lower displacement and modulus errors than XPINN. This better performance can be because DiffFEM enforces the governing equations exactly at every iteration as a hard constraint through the FEM forward solver integrated with the AD. In addition, DiffFEM is far more computationally efficient. DiffFEM converges in about 60 s, whereas XPINN required about 10 h on the same hardware.

Overall, the findings indicate that PINN-based inverse analysis should be used with caution for FWD backcalculation. For problems like layered-elastic systems, where the forward model is well established, numerically stable, and differentiable, DiffFEM is a more reliable and efficient choice. More broadly, this study suggests that in inverse problems with accessible differentiable solvers, physics-native AD formulations may offer a more practical path than PINN-based approaches, where physics-consistent solutions are not always guaranteed. Nevertheless, PINNs may remain attractive when differentiable forward solvers are unavailable, difficult to implement, computationally burdensome due to long time-stepping histories, or when mesh-free formulations offer practical advantages.

A potential direction for future work is to evaluate the framework under more realistic pavement conditions, including viscoelasticity and nonlinear constitutive behavior. These settings may introduce adaptive time stepping and non-differentiable algorithmic components, which could complicate differentiable solver construction. Whether we can make these operations differentiable to take advantage of AD remains unclear and opens opportunities for further studies.

## **7. Data and code availability**

Data and code will be made available on request.

## **8. Acknowledgment**

This work was supported by the InnoCORE program of the Ministry of Science and ICT(N10260002).

## Appendix A.

Table A.5: Quantitative inversion results across all noise levels. True moduli:  $E_{surface} = 1,378$  MPa,  $E_{base} = 206$  MPa,  $E_{subgrade} = 69$  MPa. This table is visualized as Figure 13

$\sigma$ ( $\mu\text{m}$ )	RMSE (mm)				Relative error (%)					
	$u_r$		$u_z$		$E_1$ (surface)		$E_2$ (base)		$E_3$ (subgrade)	
	DiffFEM	XPINN	DiffFEM	XPINN	DiffFEM	XPINN	DiffFEM	XPINN	DiffFEM	XPINN
0	$1.36 \times 10^{-11}$	0.00291	$3.12 \times 10^{-11}$	0.00719	$2.31 \times 10^{-7}$	1.46	$2.01 \times 10^{-7}$	2.13	$9.89 \times 10^{-8}$	14.4
1	$9.54 \times 10^{-5}$	0.00892	$1.55 \times 10^{-4}$	0.0835	2.71	74.4	1.23	66.7	$5.04 \times 10^{-2}$	94.2
2	$1.89 \times 10^{-4}$	0.00755	$3.08 \times 10^{-4}$	0.0178	5.46	92.5	2.46	122	$8.46 \times 10^{-2}$	21.1
3	$2.80 \times 10^{-4}$	0.0100	$4.59 \times 10^{-4}$	0.0224	8.26	95.6	3.69	234	$1.03 \times 10^{-1}$	14.7
4	$3.69 \times 10^{-4}$	0.0105	$6.07 \times 10^{-4}$	0.0260	11.1	96.0	4.92	245	$1.06 \times 10^{-1}$	19.2
5	$4.56 \times 10^{-4}$	0.0147	$7.53 \times 10^{-4}$	0.0381	14.0	97.2	6.15	391	$9.41 \times 10^{-2}$	42.9

## References

- Bai, J., Lin, Z., Wang, Y., Wen, J., Liu, Y., Rabczuk, T., Gu, Y., Feng, X.Q., 2025. Energy-based physics-informed neural network for frictionless contact problems under large deformation. *Computer Methods in Applied Mechanics and Engineering* 437, 117787.
- Baydin, A.G., Pearlmutter, B.A., Radul, A.A., Siskind, J.M., 2018. Automatic differentiation in machine learning: a survey. *Journal of machine learning research* 18, 1–43.
- Bekele, Y.W., 2021. Physics-informed deep learning for one-dimensional consolidation. *Journal of Rock Mechanics and Geotechnical Engineering* 13, 420–430.
- Burmister, D.M., 1945. The general theory of stresses and displacements in layered systems. i. *Journal of Applied Physics* 16, 89–94.
- Choi, Y., Kumar, K., 2024. Inverse analysis of granular flows using differentiable graph neural network simulator. *Computers and Geotechnics* 171, 106374.
- Chou, Y.E., Liu, T.H., Lin, C.A., 2025. Impact of loss weight and model complexity on physics-informed neural networks for computational fluid dynamics. *arXiv preprint arXiv:2509.21393*.
- Cuomo, S., Di Cola, V.S., Giampaolo, F., Rozza, G., Raissi, M., Piccialli, F., 2022. Scientific machine learning through physics-informed neural networks: Where we are and what’s next. *Journal of Scientific Computing* 92, 88.
- Eghbalian, M., Pouragha, M., Wan, R., 2023. A physics-informed deep neural network for surrogate modeling in classical elasto-plasticity. *Computers and Geotechnics* 159, 105472.
- Faroughi, S.A., Pawar, N.M., Fernandes, C., Raissi, M., Das, S., Kalantari, N.K., Kourosh Mahjour, S., 2024. Physics-guided, physics-informed, and physics-encoded neural networks and operators in scientific computing: Fluid and solid mechanics. *Journal of Computing and Information Science in Engineering* 24, 040802.

- Fazliani, S., Frangella, Z., Udell, M., 2025. Enhancing physics-informed neural networks through feature engineering. arXiv preprint arXiv:2502.07209 .
- Gong, W., Zuo, L., Li, L., Wang, H., 2025. Prediction of stratified ground consolidation via a physics-informed neural network utilizing short-term excess pore water pressure monitoring data. *Computer-Aided Civil and Infrastructure Engineering* 40, 147–165.
- Gopalakrishnan, K., Manik, A., 2010. Co-variance matrix adaptation evolution strategy for pavement backcalculation. *Construction and Building Materials* 24, 2177–2187.
- Harichandran, R.S., Mahmood, T., Raab, A.R., Baladi, G.Y., 1993. Modified newton algorithm for backcalculation of pavement layer properties. *Transportation Research Record* 1384, 15.
- Hou, Q., Li, Y., Singh, V.P., Sun, Z., Wei, J., 2024. Physics-informed neural network for solution of forward and inverse kinematic wave problems. *Journal of Hydrology* 633, 130934.
- Hu, Y., Anderson, L., Li, T.M., Sun, Q., Carr, N., Ragan-Kelley, J., Durand, F., 2019. DiffTaichi: Differentiable programming for physical simulation. arXiv preprint arXiv:1910.00935 .
- Innes, M., Edelman, A., Fischer, K., Rackauckas, C., Saba, E., Shah, V.B., Tebbutt, W., 2019. A differentiable programming system to bridge machine learning and scientific computing. arXiv preprint arXiv:1907.07587 .
- Jagtap, A.D., Karniadakis, G.E., 2020. Extended physics-informed neural networks (xpinns): A generalized space-time domain decomposition based deep learning framework for nonlinear partial differential equations. *Communications in Computational Physics* 28.
- Kumar, K., 2025. Deep learning in geotechnical engineering: A critical assessment of pinns and operator learning. arXiv preprint arXiv:2512.24365 .
- Kumar, S.K., 2017. On weight initialization in deep neural networks. arXiv preprint arXiv:1704.08863 .
- Kuo, C.M., Chou, F.J., 2004. Development of 3-d finite element model for flexible pavements. *Journal of the Chinese Institute of Engineers* 27, 707–717.
- Li, Z., Bai, J., Ouyang, H., Martelli, S., Tang, M., Yang, Y., Wei, H., Liu, P., Wei, R., Gu, Y., 2024. Physics-informed neural networks for friction-involved nonsmooth dynamics problems. *Nonlinear Dynamics* 112, 7159–7183.
- Liu, C., Macedo, J., Rodriguez, A., 2025. Leveraging physics-informed neural networks in geotechnical earthquake engineering: An assessment on seismic site response analyses. *Computers and Geotechnics* 182, 107137.
- Liu, D.C., Nocedal, J., 1989. On the limited memory bfgs method for large scale optimization. *Mathematical programming* 45, 503–528.
- Margossian, C.C., 2019. A review of automatic differentiation and its efficient implementation. *Wiley interdisciplinary reviews: data mining and knowledge discovery* 9, e1305.
- McClenny, L.D., Braga-Neto, U.M., 2023. Self-adaptive physics-informed neural networks. *Journal of Computational Physics* 474, 111722. doi:10.1016/j.jcp.2022.111722.
- Meier, R.W., Rix, G.J., 1994. Backcalculation of flexible pavement moduli using artificial neural networks. *Transportation research record* .

- Moon, H., Park, D., Cho, H., Noh, H.K., Lim, J.H., Ryu, S., 2025. Physics-informed neural network-based discovery of hyperelastic constitutive models from extremely scarce data. *Computer Methods in Applied Mechanics and Engineering* 446, 118258.
- Naser, M., 2025. Fundamental flaws of physics-informed neural networks and explainability methods in engineering systems. *Computers & Industrial Engineering* , 111704.
- Paszke, A., Gross, S., Chintala, S., Chanan, G., Yang, E., DeVito, Z., Lin, Z., Desmaison, A., Antiga, L., Lerer, A., 2017. Automatic differentiation in pytorch .
- Paulus, A., Geist, A.R., Musil, V., Hoffmann, S., Beker, O., Martius, G., 2026. Softjax & softtorch: Empowering automatic differentiation libraries with informative gradients. *arXiv preprint arXiv:2603.08824* .
- Peng, B., Panesar, A., 2025. Multi-layer thermal history prediction framework for directed energy deposition based on extended physics-informed neural networks (xpinn). *Additive Manufacturing* , 104953.
- Press, W.H., Teukolsky, S.A., Vetterling, W.T., Flannery, B.P., 2007. *Numerical Recipes: The Art of Scientific Computing*. 3 ed., Cambridge University Press, Cambridge, UK.
- Raissi, M., Perdikaris, P., Karniadakis, G.E., 2019. Physics-informed neural networks: A deep learning framework for solving forward and inverse problems involving nonlinear partial differential equations. *Journal of Computational physics* 378, 686–707.
- Rasht-Behesht, M., Huber, C., Shukla, K., Karniadakis, G.E., 2022. Physics-informed neural networks (pinns) for wave propagation and full waveform inversions. *Journal of Geophysical Research: Solid Earth* 127, e2021JB023120.
- Rathore, P., Lei, W., Frangella, Z., Lu, L., Udell, M., 2024. Challenges in training pinns: A loss landscape perspective. *arXiv preprint arXiv:2402.01868* .
- Rohde, G.T., Scullion, T., 1990. *Modulus 4.0: Expansion and Validation of the Modulus Backcalculation System*. Technical Report FHWA/TX-91/1123-3. Texas Transportation Institute, Texas A&M University. URL: <https://rosap.nrl.bts.gov/view/dot/86281>. prepared for Texas State Department of Highways and Public Transportation and the Federal Highway Administration, U.S. Department of Transportation.
- Rowan, C., Murphy-Blanchard, F., 2026. Visualizing the loss landscapes of physics-informed neural networks. *arXiv preprint arXiv:2602.05849* .
- Sahin, T., von Danwitz, M., Popp, A., 2024. Solving forward and inverse problems of contact mechanics using physics-informed neural networks. *Advanced Modeling and Simulation in Engineering Sciences* 11, 11.
- Smith, K.D., Bruinsma, J.E., Wade, M.J., Chatti, K., Vandenbossche, J., Yu, H.T., 2017. Using Falling Weight Deflectometer Data With Mechanistic-Empirical Design and Analysis, Volume I: Final Report. Technical Report FHWA-HRT-16-009; HRDI-20/03-17(WEB)E. Applied Pavement Technology, Inc.. United States. URL: <https://rosap.nrl.bts.gov/view/dot/37574>. prepared for the Federal Highway Administration.
- Sukumar, N., Srivastava, A., 2022. Exact imposition of boundary conditions with distance functions in physics-informed deep neural networks. *Computer Methods in Applied Mechanics and Engineering* 389, 114333.
- Tarefder, R.A., Ahmed, M.U., 2014. Modeling of the fwd deflection basin to evaluate airport pavements. *International*

Journal of Geomechanics 14, 205–213.

- Von Quintus, H.L., Rao, C., Irwin, L., 2015. Long-Term Pavement Performance Program Determination of In-Place Elastic Layer Modulus: Backcalculation Methodology and Procedures. FHWA Research Report FHWA-HRT-15-036. Federal Highway Administration, McLean, VA. URL: <https://www.fhwa.dot.gov/publications/research/infrastructure/pavements/ltp/15036/index.cfm>. office of Infrastructure Research and Development.
- Wang, S., Teng, Y., Perdikaris, P., 2021. Understanding and mitigating gradient flow pathologies in physics-informed neural networks. *SIAM Journal on Scientific Computing* 43, A3055–A3081.
- Yuan, B., Choo, C.S., Yeo, L.Y., Wang, Y., Yang, Z., Guan, Q., Suryasentana, S., Choo, J., Shen, H., Megia, M., et al., 2025. Physics-informed machine learning in geotechnical engineering: a direction paper. *Geomechanics and Geoengineering* 20, 1128–1159.
- Zhang, Z., Manuel, L., Damnjanovic, I., Li, Z., et al., 2003. Development of a new methodology for characterizing pavement structural condition for network-level applications. Texas Dept. of Transportation, Austin, TX .